The Gas and Stellar Content of a Metal-poor Galaxy at z = 8.496 as Revealed by JWST and ALMA

K. Heintz, C. Giménez-Arteaga, S. Fujimoto, G. Brammer, D. Espada, S. Gillman, J. González-López, T. Greve, Y. Harikane, B. Hatsukade, et al.

The Astrophysical Journal Letters, 944:L30 (13pp), 2023 February 20 https://doi.org/10.3847/2041-8213/acb2cf

The Gas and Stellar Content of a Metal-poor Galaxy at $z = 8.496$ as Revealed by JWST and ALMA

K. E. Heintz[1,2], C. Giménez-Arteaga[1,2], S. Fujimoto[1,2,3], G. Brammer[1,2], D. Espada[4,5], S. Gillman[1,6], J. González-López[7,8], T. R. Greve[1,6], Y. Harikane[9], B. Hatsukade[10], K. K. Knudsen[11], A. M. Koekemoer[12], K. Kohno[10,13], V. Kokorev[14], M. M. Lee[1,6], G. E. Magdis[1,2,6], E. J. Nelson[15], F. Rizzo[1,2], R. L. Sanders[16,17], D. Schaerer[18,19], A. E. Shapley[16], V. B. Strait[1,2], S. Toft[1,2], F. Valentino[1,2,20], A. van der Wel[21], A. P. Vijayan[1,6], D. Watson[1,2], F. E. Bauer[22,23,24], C. R. Christiansen[1,2], and S. N. Wilson[1,2]

[1] Cosmic Dawn Center (DAWN), Denmark; keheintz@nbi.ku.dk
[2] Niels Bohr Institute, University of Copenhagen, Jagtvej 128, DK-2200 Copenhagen N, Denmark
[3] Department of Astronomy, The University of Texas at Austin, Austin, TX 78712, USA
[4] Departamento de Física Teórica y del Cosmos, Campus de Fuentenueva, Edificio Mecenas, Universidad de Granada, E-18071, Granada, Spain
[5] Instituto Carlos I de Física Teórica y Computacional, Facultad de Ciencias, E-18071, Granada, Spain
[6] DTU-Space, Technical University of Denmark, Elektrovej 327, DK-2800, Kgs. Lyngby, Denmark
[7] Las Campanas Observatory, Carnegie Institution of Washington, Casilla 601, La Serena, Chile
[8] Núcleo de Astronomía, Facultad de Ingeniería y Ciencias, Universidad Diego Portales, Av. Ejército Libertador 441, Santiago, Chile
[9] Institute for Cosmic Ray Research, The University of Tokyo, 5-1-5 Kashiwanoha, Kashiwa, Chiba 277-8582, Japan
[10] Institute of Astronomy, Graduate School of Science, The University of Tokyo, 2-21-1 Osawa, Mitaka, Tokyo 181-0015, Japan
[11] Department of Space, Earth and Environment, Chalmers University of Technology, Onsala Space Observatory, SE-439 92 Onsala, Sweden
[12] Space Telescope Science Institute, 3700 San Martin Dr., Baltimore, MD 21218, USA
[13] Research Center for the Early Universe, Graduate School of Science, The University of Tokyo, 7-3-1 Hongo, Bunkyo-ku, Tokyo 113-0033, Japan
[14] Kapteyn Astronomical Institute, University of Groningen, PO Box 800, 9700 AV Groningen, The Netherlands
[15] Department for Astrophysical and Planetary Science, University of Colorado, Boulder, CO 80309, USA
[16] Department of Physics and Astronomy, University of California, Los Angeles, 430 Portola Plaza, Los Angeles, CA 90095, USA
[17] Department of Physics, University of California, Davis, 1 Shields Ave., Davis, CA 95616, USA
[18] Observatoire de Genève, Université de Genève, Chemin Pegasi 51, 1290 Versoix, Switzerland
[19] CNRS, IRAP, 14 Ave. E. Belin, F-31400 Toulouse, France
[20] European Southern Observatory, Karl-Schwarzschild-Str. 2, D-85748 Garching bei Munchen, Germany
[21] Sterrenkundig Observatorium, Universiteit Gent, Krijgslaan 281 S9, B-9000 Gent, Belgium
[22] Instituto de Astrofísica, Facultad de Física, Pontificia Universidad Católica de Chile, Campus San Joaquín, Av. Vicuña Mackenna 4860, Macul Santiago, 7820436, Chile
[23] Centro de Astroingeniería, Facultad de Física, Pontificia Universidad Católica de Chile, Campus San Joaquín, Av. Vicuña Mackenna 4860, Macul Santiago, 7820436, Chile
[24] Millennium Institute of Astrophysics, Nuncio Monse nor Sótero Sanz 100, Of. 104, Providencia, Santiago, Chile
Received 2022 December 13; revised 2023 January 9; accepted 2023 January 13; published 2023 February 15

Abstract

We present a joint analysis of the galaxy S04590 at $z = 8.496$ based on NIRSpec, NIRCam, and NIRISS observations obtained as part of the Early Release Observations program of the James Webb Space Telescope (JWST) and the far-infrared [C II] 158 μm emission line detected by dedicated Atacama Large Millimeter/submillimeter Array (ALMA) observations. We determine the physical properties of S04590 from modeling of the spectral energy distribution (SED) and through the redshifted optical nebular emission lines detected with JWST/NIRSpec. The best-fit SED model reveals a low-mass ($M_\star = 10^{7.2}$–$10^8\,M_\odot$) galaxy with a low oxygen abundance of $12 + \log(\mathrm{O/H}) = 7.16^{+0.10}_{-0.12}$ derived from the strong nebular and auroral emission lines. Assuming that [C II] effectively traces the interstellar medium, we estimate the total gas mass of the galaxy to be $M_{\rm gas} = (8.0 \pm 4.0) \times 10^8\,M_\odot$ based on the luminosity and spatial extent of [C II]. This yields an exceptionally high gas fraction, $f_{\rm gas} = M_{\rm gas}/(M_{\rm gas} + M_\star) \gtrsim 90\%$, though one still consistent with the range expected for low metallicity. We further derive the metal mass of the galaxy based on the gas mass and gas-phase metallicity, which we find to be consistent with the expected metal production from Type II supernovae. Finally, we make the first constraints on the dust-to-gas (DTG) and dust-to-metal (DTM) ratios of galaxies in the epoch of reionization at $z \gtrsim 6$, showing overall low mass ratios of $\log\mathrm{DTG} < -3.8$ and $\log\mathrm{DTM} < -0.5$, though they are consistent with established scaling relations and in particular with those of the local metal-poor galaxy I Zwicky 18. Our analysis highlights the synergy between ALMA and JWST in characterizing the gas, metal, and stellar content of the first generation of galaxies.

Unified Astronomy Thesaurus concepts: High-redshift galaxies (734); Galaxies (573); Interstellar medium (847); Star formation (1569); Galaxy formation (595); Galaxy evolution (594)

1. Introduction

The first epoch of galaxy formation is believed to have occurred at $z \sim 15$–20 (Hashimoto et al. 2018; Robertson 2022), some 100–200 million years after the Big Bang. This process was initiated by the infall of pristine, neutral gas onto the first

protogalactic halos, which would eventually cool and condense into H_2 gas reservoirs and later form stars (Dayal & Ferrara 2018). Ending their lives as core-collapse supernovae, the first generation of stars enriched the pristine gas with dust and metals, providing the material for subsequent star formation and thus galaxy evolution heralding the epoch of reionization. It is therefore vital to probe the interstellar medium (ISM) and dust and metal buildup in galaxies at $z \gtrsim 6$ to constrain the star formation histories (SFHs) of the first galaxies.

The Atacama Large Millimeter/submillimeter Array (ALMA) has been paramount in providing a clear census of the rest-frame far-infrared (FIR) emission of galaxies at $z \gtrsim 6$. The fine-structure $^2P_{3/2}-^2P_{1/2}$ [C II] 158 μm line transition in particular, which is one of the major ISM cooling lines (Hollenbach & Tielens 1999; Wolfire et al. 2003; Carilli & Walter 2013; Lagache et al. 2018), has been used to infer the ISM dynamics (Capak et al. 2015; Smit et al. 2018; Matthee et al. 2019) and overall gas content (Knudsen et al. 2016; Dessauges-Zavadsky et al. 2020; Heintz et al. 2021, 2022a; M. Aravena et al. 2023, in preparation) of individual galaxies at $z \gtrsim 6$. In more local galaxies at $z \approx 0$, [C II] has been linked to the star formation rate (SFR) (Stacey et al. 1991; De Looze et al. 2014; Cormier et al. 2015) and physically associated with the neutral, atomic gas and photodissociation regions (Madden et al. 1993, 1997; Hollenbach & Tielens 1999). The relationship between the SFR and the luminosity of [C II], $L_{[\mathrm{CII}]}$, has been shown to be universally valid out to $z \approx 8$ (Schaerer et al. 2020). Further, the [C II] halos surrounding these early galaxies, which typically extend 2–3$\times$ beyond their UV components (e.g., Smit et al. 2018; Fujimoto et al. 2019; Matthee et al. 2019; Carniani et al. 2020; Fudamoto et al. 2022), are reminiscent of the extended [C II] emission originating from the neutral, atomic hydrogen (H I) gas phase in local galaxies (Madden et al. 1993). FIR continuum emission (Draine & Li 2007; Scoville et al. 2014) has further enabled strong constraints on the dust mass and temperature of galaxies at $z \gtrsim 6$ (Bakx et al. 2021; Sommovigo et al. 2021; Algera et al. 2023; Dayal et al. 2022; Ferrara et al. 2022; Inami et al. 2022; Sommovigo et al. 2022). Thus, we now have a robust census of the dust and gas properties of galaxies well into the epoch of reionization.

The final missing ingredient to understand and fully characterize the ISM is thus the metal abundance and the overall chemical enrichment of the galaxies at this early epoch. Strong-line diagnostics of the most prominent nebular emission lines have been used as viable tools to infer the gas-phase metallicities (Kewley & Ellison 2008; Kewley et al. 2019; Maiolino & Mannucci 2019), typically calibrated to the more direct T_e method. However, these measurements have previously been limited by the atmospheric cutoff for ground-based observations and have as a result mostly been possible to derive robustly only for galaxies up to $z \approx 3$ (Christensen et al. 2012; Sanders et al. 2021). Chemical abundances have also been derived for foreground galaxies toward background sources such as gamma-ray bursts and quasars out to $z \gtrsim 6$ (Hartoog et al. 2015; Simcoe et al. 2020; Saccardi et al. 2022), which, however, only represent a single line of sight through the absorbing galaxies.

Now with the advent of JWST we are able to derive robust, total gas-phase metallicities through the strong-line diagnostics of the most prominent nebular emission lines of galaxies during the first Gyr of cosmic time (e.g., Curti et al. 2023; Heintz et al. 2022b; Rhoads et al. 2023; Schaerer et al. 2022; Tacchella et al. 2022). Crucially, these observations have also revealed prominent detections of the auroral [O III] λ4363 emission line, which enables direct T_e-based metallicity measurements, which is necessary to consider since the typical strong-line diagnostics have only been calibrated to local $z \approx 0$ galaxy samples. JWST and ALMA thus jointly provide a unique and comprehensive view of the gas, dust, and metal content of the first galaxies. While the first such combined studies of some of the highest-redshift galaxy candidates identified by JWST remain inconclusive (Bakx et al. 2023; Fujimoto et al. 2022a; Popping 2023; Yoon et al. 2022), it is still not entirely clear whether this is due to their likely low metallicities or to their potentially erroneous photometric redshifts.

Here we present a characterization of the stellar, gas, and metal content of a galaxy at $z \approx 8.5$, from a joint analysis of observations obtained with JWST and ALMA. Hereafter, we refer to this galaxy as S04590, based on its ID in JWST/NIRSPEC mask design. The JWST data, including observations taken with the Near-infrared Spectrograph (NIRSpec), the Near-infrared Camera (NIRCam), and the Near Infrared Imager and Slitless Spectrograph (NIRISS), are from the early-release science observations (ERO) covering the SMACS J0723.3-7327 galaxy cluster (see Pontoppidan et al. 2022). The ALMA observations were presented in detail by Fujimoto et al. (2022b), who reported the detections of the FIR emission lines [O III] 88 μm and [C II] 158 μm of S04590. This galaxy thus also presents the most distant detection of the [C II] 158 μm line transition feature to date, and greatly highlights the importance of having robust, spectroscopic redshifts from JWST to optimize follow-up at FIR wavelengths with ALMA.

We structure the paper as follows. In Section 2 the observations are detailed and in Section 3 we present and analyze the results. In Section 4 we infer the gas and metal content and discuss the implications of this work and in Section 5 we highlight the great synergy between JWST and ALMA, and provide some concluding remarks. Throughout the paper we quote magnitudes in the AB system and adopt the concordance ΛCDM cosmological model with $\Omega_m = 0.315$, $\Omega_\Lambda = 0.685$, and $H_0 = 67.4$ km s^{-1} Mpc^{-1} (Planck Collaboration et al. 2020). We assume a Chabrier (2003) initial mass function (IMF) and the solar abundances from Asplund et al. (2009) with $Z_\odot = 0.0134$.

2. Observations

2.1. NIRCam and NIRISS Photometry

We include the JWST NIRCam and NIRISS photometric data of S04590 from the catalog presented by G. Brammer et al. (2023, in preparation), which provides a compilation of the JWST ERO photometric data released to date. Briefly, the raw data entered into this catalog has been reduced using the public software package `grizli` (Brammer 2019), which masks imaging artifacts, provides astrometric calibrations based on the Gaia Data Release 3 catalog, and shifts images to a common pixel scale of 0.″04 pixel^{-1} using `astrodrizzle`. Cutouts of the reduced images from NIRCam and NIRISS used in this analysis are provided on a dedicated repository.[27] S04590 is detected in the five deep NIRCam

[27] https://github.com/keheintz/S04590

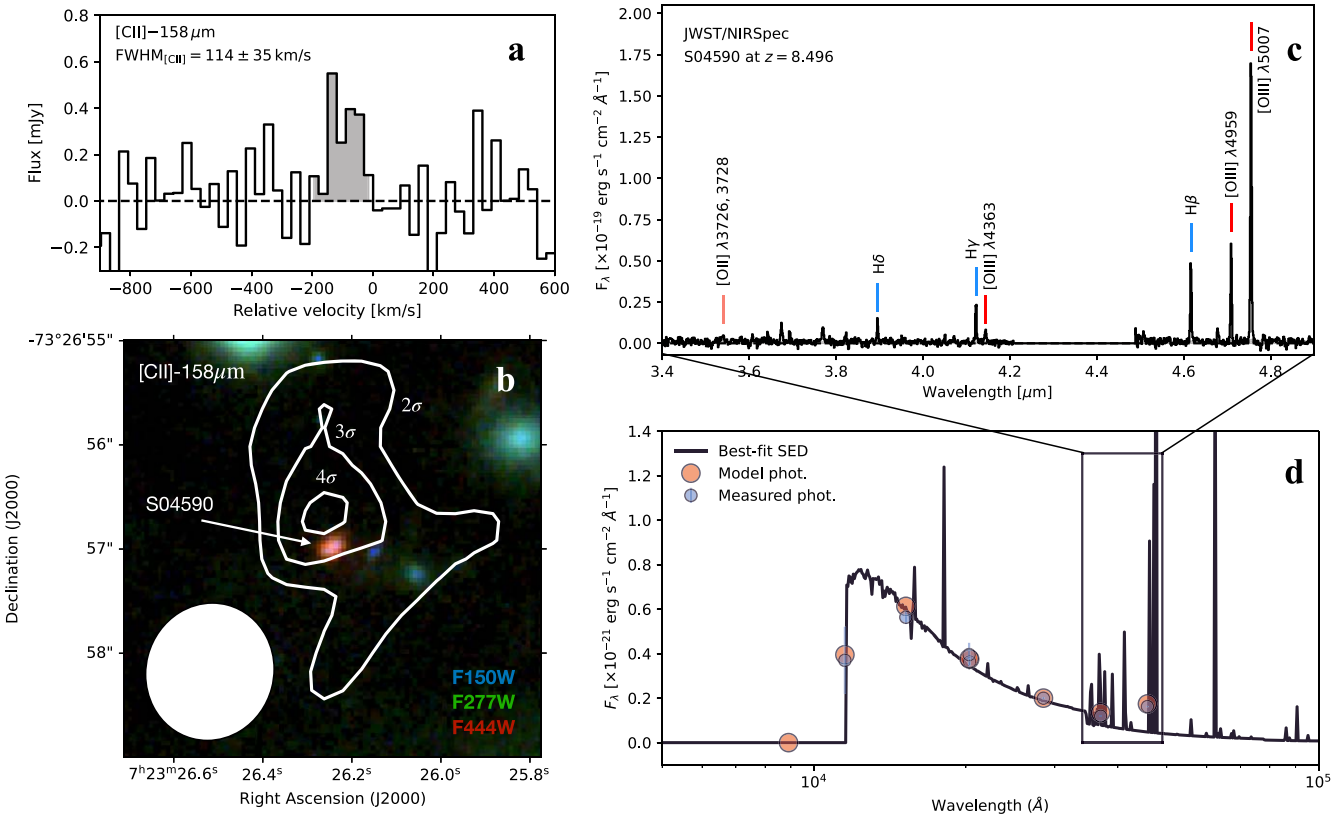

Figure 1. Panel (a): [C II] line spectrum from the 30 km s^{-1} ALMA data cube (Fujimoto et al. 2022b). Panel (b): False-color RGB JWST/NIRCam image zoomed in on S04590 (blue: F150W; green: F277W; red: F444W), overlaid with the 2σ, 3σ, and 4σ contours of the [C II] moment-0 map with the beam size represented by the white ellipse. Panel (c): JWST/NIRSpec spectrum with the most prominent nebular and auroral emission lines marked. Panel (d): Best-fit SED model (black curve) and model photometry (red points) based on the derived JWST/NIRCam+NIRISS photometry (blue points) using BAGPIPES (Carnall et al. 2018) and assuming the dust attenuation curve from Salim et al. (2018).

imaging filters F150W, F200W, F277W, F356W, and F444W, with an F150W ($\approx H$-band) magnitude = 27.3. The nondetection in the bluest filter F090W makes this galaxy a clear photometric dropout. We also include two shallower images obtained with NIRISS with the F115W and F200W filters. This set of photometric measurements is derived using the updated zero-points, and corrected for Milky Way extinction. Since the source is extended in the images, we use aperture photometry derived using a diameter of 0.″5 from the catalog by G. Brammer et al. (2023, in preparation).

The centroid of the galaxy is localized to R.A., decl. = $7^{\rm h}23^{\rm m}26\overset{\rm s}{.}24$, $-73°26'57\overset{''}{.}0$. A zoomed-in image showing the false RGB color (F150W+F277W+F444W) of S04590 is shown in Figure 1, together with the spectral energy distribution (SED) inferred from modeling of the photometric data points (see also Section 3.2).

2.2. NIRSpec Spectroscopy

The JWST ERO spectroscopic data of S04590 have already been presented and examined by a number of independent studies (Arellano-Córdova et al. 2022; Brinchmann 2022; Carnall et al. 2023; Curti et al. 2023; Katz et al. 2023; Rhoads et al. 2023; Schaerer et al. 2022; Tacchella et al. 2022; Taylor et al. 2022; Trump et al. 2022). The NIRSpec spectroscopy is obtained with the medium-resolution gratings G235M/F170LP (1.75–3.1 μm) and G395M/F290LP (2.9–5.2 μm), with $\mathcal{R} = \lambda/\Delta\lambda = 1000$ (Jakobsen et al. 2022), for a total exposure time of 8754 s. We use the JWST pipeline to perform the standard wavelength, flat-field, and photometric calibrations to the individual NIRSpec exposure files.[28] We generate the full combined 2D spectra and optimal (Horne 1986) 1D extractions with scripts that extend the standard pipeline functionality (Brammer 2022). We further scale the overall flux density of the spectrum to the derived photometry to improve the absolute flux calibration by matching the integrated flux within the F444W passband to the derived photometry of the same filter. The reduced spectrum is made available on the dedicated repository.[27] Overall, our extracted version of the spectrum appears consistent with the publicly available 1D spectrum from Curti et al. (2023), though we detect a slightly weaker [O II] $\lambda\lambda$3726, 3729 doublet and [O III] λ4363 line transition (see Section 3.3 for further discussion). We confirm a similar trend in another up-to-date NIRSpec study in Nakajima et al. (2023). Both of these spectra were derived from an independent source extraction and calibration, which alleviated the issues regarding flux calibration and the inferred line ratios from the Phase 3 MAST products due to an error in the first s007 exposure. The spectrum is presented in Figure 1, where the most prominent nebular emission lines used to determine the redshift and infer the physical properties of the galaxy are marked as well.

2.3. ALMA Observations

ALMA Band 5 follow-up observations of [C II] spectroscopy were performed as a part of the Cycle 8 DDT program (#2022.

[28] Calibration levels 1 and 2 with `jwst` version 1.8.2.

A.00022.S, PI: S. Fujimoto). The details of the observations, data reduction, calibrations, and imaging procedures are presented in Fujimoto et al. (2022b). Briefly, we reduced and calibrated the ALMA data with the Common Astronomy Software Applications package version 6.4.1.12 (CASA; McMullin et al. 2007) by using the pipeline script in the standard manner. We adopted the natural weighting, resulting in an FWHM size of the synthesized beam of $1\farcs35 \times 1\farcs25$ with 1σ sensitivities for the continuum map and the line cube with a 40 km s^{-1} channel width of 11.6 μJy beam^{-1} and 165 μJy beam^{-1}, respectively.

The [C II] line emission originating from S04590 is detected at 4.5σ, but is blueshifted by 90 km s^{-1} from the rest-frame optical spectrum and with a spatial offset of $0\farcs5$ from the rest-frame UV component (Fujimoto et al. 2022b; see also Figure 1). The robustness of the detection is substantiated by the simultaneous detection of the FIR [O III] 88 μm emission line, which, however, is spatially and spectroscopically consistent with the UV, star-forming component.

The [C II] line is detected with a velocity-integrated flux of $S_{[\mathrm{CII}]} = 0.094 \pm 0.027$ Jy km s^{-1}. This corresponds to an intrinsic luminosity (following, e.g., Solomon & Vanden Bout 2005) of $L_{[\mathrm{CII}]} = (1.67 \pm 0.37) \times 10^7\, L_\odot$, corrected for the magnification factor due to gravitational lensing, which we here assume to be $\mu = 8.69$ from the updated GLAFIC lens model (Harikane et al. 2022). We note the 10%–30% differences among the most recent mass models for this cluster (Caminha et al. 2022; Mahler et al. 2022). To represent this uncertainty and for internal consistency with Fujimoto et al. (2022b) we adopt $\mu = 8.69 \pm 2.61$ here. Modeling the [C II] emission line in the 1D spectrum extracted from the higher-resolution data cube, with a resolution of 30 km s^{-1}, yields an $\mathrm{FWHM}_{[\mathrm{CII}],\mathrm{obs}} = 118 \pm 36$ km s^{-1} (Fujimoto et al. 2022b), or a line width of $\sigma_{[\mathrm{CII}],\mathrm{obs}} = 50 \pm 15$ km s^{-1}. Correcting for the instrumental resolution this corresponds to an intrinsic line width of $\mathrm{FWHM}_{[\mathrm{CII}],\mathrm{intr}} = \sqrt{\mathrm{FWHM}^2_{[\mathrm{CII}],\mathrm{obs}} - \mathrm{FWHM}^2_{\mathrm{inst}}} = 114 \pm 35$ km s^{-1}, as reported in Table 1 and used throughout.

Table 1
Measurements and Physical Properties of S04590

R.A. (J2000)	07:23:26.24 (110.°85933)
Decl. (J2000)	−73:26:57.0 (−73.°44917)
z_{spec}	8.4959 ± 0.0003
[a]$\log(M_\star/M_\odot)$	7.15 ± 0.15
[a]Mean stellar age (Myr)	$1.3^{+0.4}_{-0.3}$
[a]A_V (mag)	$0.20^{+0.04}_{-0.03}$
[a]$\log_{10}(U)$	$-1.12^{+0.08}_{-0.18}$
[a]β_{UV}	-1.81 ± 0.08
[b]$S_{[\mathrm{CII}]}$ (Jy km s^{-1})	$(1.1 \pm 0.3) \times 10^{-2}$
[b]$L_{[\mathrm{CII}]}$ ($L_\odot$)	$(1.67 \pm 0.37) \times 10^7$
$\sigma_{[\mathrm{CII}]}$ (km s^{-1})	50 ± 15
$\mathrm{FWHM}_{[\mathrm{CII}]}$ (km s^{-1})	114 ± 35
$\mathrm{SFR}_{\mathrm{H}\beta}$ ($M_\odot$ yr^{-1})	2.9 ± 0.9
T_e (K)	$(2.4 \pm 0.4) \times 10^4$
$12 + \log(\mathrm{O/H})$	$7.16^{+0.10}_{-0.12}$
$\log Z/Z_\odot$	$-1.53^{+0.10}_{-0.12}$
$M_{\mathrm{dyn,tot}}$ ($M_\odot$)	$(9.0 \pm 4.5) \times 10^8$
M_{gas} ($M_\odot$)	$(8.0 \pm 4.0) \times 10^8$
$M_{\mathrm{Z,ISM}}$ ($M_\odot$)	$(3.2 \pm 1.6) \times 10^5$
[b]M_d ($M_\odot$)	$<1.2 \times 10^5$

Notes. All values reported here that are affected by magnification due to gravitational lensing have been corrected by the magnification factor $\mu = 8.69$.
[a] Inferred physical properties from the SED model are based on the integrated photometry (see text for caveats).
[b] Measurements from Fujimoto et al. (2022b).

3. Results and Analysis

3.1. Morphology and Galaxy Size

We first model the morphology of S04590 in all the NIRCam images in which it is detected (excluding F090W) simultaneously using GALFIT (Peng et al. 2002). We find that a simple Sersíc profile is able to reproduce the observed light profile, with an effective radius around 1.5–2 pixels depending on the filter used. In the F150W filter (rest-frame UV ≈1600 Å) we derive an effective radius of $r_{\mathrm{e,UV}} = 0\farcs07$, corresponding to $r_{\mathrm{e,UV}} = 0.33$ kpc in the image plane at $z = 8.496$ (consistent with the results of Rhoads et al. 2023). Correcting for the magnification factor, we estimate a physical size of $r_{\mathrm{e,UV}}/\sqrt{\mu} = 0.11$ kpc in the source plane.

3.2. Modeling the SED

To infer the physical properties as well as constrain the SFH of S04590, we model the integrated SED using the fitting code BAGPIPES (Carnall et al. 2018). We fix the redshift to the spectroscopic NIRSpec redshift $z_{\mathrm{spec}} = 8.496$ (see Section 3.3). We include nebular emission via CLOUDY (Ferland et al. 2017), allowing the ionization parameter, U, to vary within $-3 < \log_{10}(U) < -1$ to account for the typically higher ionization parameter at $z \gtrsim 6$ (Sugahara et al. 2022), and the derived electron temperature (see, e.g., Arellano-Córdova et al. 2022; Curti et al. 2023; Katz et al. 2023; Trump et al. 2022; and the section below). We assume a Salim et al. (2018) attenuation curve, which is notably steeper than the typically adopted Calzetti extinction curve (Calzetti et al. 2000). The steeper Salim et al. (2018) curve better represents low-mass, low-metallicity galaxies (Reddy et al. 2018) and effectively outputs a lower A_V. We use a constant SFH model, which mimics a bursty SFH on short timescales, expected for young galaxies at this redshift. A more detailed description of the priors used in the modeling, together with the resulting posterior distributions, is provided in Appendix A.

The best-fit SED model based on the integrated photometry shown in Figure 1 yields a stellar mass $\log_{10}(M_\star/M_\odot) = 7.15 \pm 0.15$, a young stellar population with a mean stellar age of $1.3^{+0.4}_{-0.3}$ Myr, a relatively blue UV continuum slope $\beta = -1.81 \pm 0.08$, and a low dust attenuation $A_V = 0.20^{+0.04}_{-0.03}$ mag for S04590, as summarized in Table 1. This is overall consistent with the results from Carnall et al. (2023). We note that Giménez-Arteaga et al. (2022) found a substantially higher stellar mass of $M_\star \approx 10^8\, M_\odot$ based on a resolved SED study of a set of galaxies at $z \gtrsim 5$ (including S04590), which has also been recovered assuming a burstier SFH (Tacchella et al. 2022). To take into account any potential systematic uncertainties on the stellar mass estimates from varying SFH models (Whitler et al. 2023) or in general across SED fitting codes (Pacifici et al. 2022), we assume a more conservative stellar mass of $M_\star = 10^{7.2}$–$10^{8.0}\, M_\odot$ in the following analysis.

3.3. Rest-frame Nebular Line Emission and Metallicity

Based on the extracted 1D NIRSpec spectrum, we derive the line fluxes of the following nebular and auroral emission lines: [O III] λλλ4363, 4959, 5007; the doublet [O II] λλ3726, 3729;

and the Balmer lines Hδ, Hγ, and Hβ (as also highlighted in Figure 1). We note that He I and [Ne III] have also been detected in the spectrum of S04590 (e.g., Carnall et al. 2023; Schaerer et al. 2022), but we focus on the above transitions, which are used in the primary analysis to infer the physical properties of S04590. For each line we derive the fluxes by modeling them with Gaussian profiles, keeping each flux as a free parameter but tying the redshift and the FWHM broadening together across transitions. This effectively assumes that all the nebular lines originate from the same H II region within the galaxy. In the following, however, we only consider the line ratios of transitions close together in wavelength space to minimize the propagation of any potential offsets in flux calibration in the derived results. The regions of the spectrum zoomed in on for these particular transitions with the best-fit models included are provided in Appendix B.

From the joint fit, we measure a redshift of $z = 8.4959 \pm 0.0003$. The derived Balmer line ratio, Hγ/H$\beta = 0.54 \pm 0.04$, which is consistent with the theoretically predicted ratio for a Case B recombination scenario (Osterbrock & Ferland 2006), further implies a low dust attenuation in S04590 as revealed by the best-fit SED model. We infer the SFR based on the Hβ flux measurements as

$$\mathrm{SFR}_{\mathrm{H}\beta}(M_\odot\ \mathrm{yr}^{-1}) = 5.5 \times 10^{-42} L_{\mathrm{H}\beta}(\mathrm{erg\ s}^{-1}) \times f_{\mathrm{H}\alpha/\mathrm{H}\beta}, \quad (1)$$

assuming a Kroupa (2001) IMF and the predicted $f_{\mathrm{H}\alpha/\mathrm{H}\beta} = 2.76$ from the Case B recombination scenario (at $T_e = 20{,}000$ K). We derive an intrinsic SFR of $\mathrm{SFR}_{\mathrm{H}\beta} = 2.9 \pm 0.9\ M_\odot\ \mathrm{yr}^{-1}$ based on the photometrically calibrated spectrum and taking into account the magnification factor. The derived SFR and stellar mass are consistent with the star-forming main sequence implied by the parameterization of Speagle et al. (2014) when extrapolated to $z = 8.5$, in addition to recent results presenting the SFR–$M_\star$ main sequence of galaxies at $z \sim 7$–10 (Heintz et al. 2022b). Additionally, the specific SFR ($\mathrm{sSFR} = \mathrm{SFR}/M_\star$) of $\log \mathrm{sSFR} = -6.7 \pm 0.4\ \mathrm{yr}^{-1}$ is consistent with recent estimates of galaxies at $z \gtrsim 7$ (Stefanon et al. 2022; Topping et al. 2022) and the observed redshift evolution of sSFR(z) out to $z \sim 8.5$.

To determine the electron temperature T_e and the gas-phase metallicity through the oxygen abundance 12 + log(O/H) we follow the prescriptions by Izotov et al. (2006). We derive $T_e = (2.4 \pm 0.4) \times 10^4$ K and $12 + \log(\mathrm{O/H}) = 7.16^{+0.10}_{-0.12}$ (i.e., $\log Z/Z_\odot = -1.53$, assuming $12 + \log(\mathrm{O/H})_\odot = 8.69$; Asplund et al. 2009) for all $n_e \lesssim 10^4$ cm^{-3}, which is well beyond the inferred electron densities of H II regions in local galaxies (Hunt & Hirashita 2009) and of galaxies at higher redshifts ($n_e \approx 10^2$ cm^{-3}; Gillman et al. 2022). Fujimoto et al. (2022b) also found $n_e = 220^{+170}_{-100}$ cm^{-3} for S04590 directly from the [O III] 88 μm/λ5007 line ratio. Our results are generally consistent with previous estimates (Arellano-Córdova et al. 2022; Brinchmann 2022; Curti et al. 2023; Rhoads et al. 2023; Schaerer et al. 2022; Trump et al. 2022), though we note the slightly lower T_e and higher 12 + log(O/H), which represent the weaker [O II] $\lambda\lambda$3726, 3729 and [O III] λ4363 line transitions detected in our extracted version of the spectrum. The oxygen abundance is found to be dominated by O^{2+}, with only a small contribution from O^+. We further note that the ratio [O III] λ5007/H$\beta = 3.65 \pm 0.11$ places S04590 in the upper region of the Baldwin–Phillips–Terlevich diagram (Baldwin et al. 1981), suggesting high ionization parameters from harder ionization fields or potential active galactic nucleus contributions. The narrow emission lines seem to exclude the latter, however. Our results thus mainly point to S04590 being a dense, highly ionized star-forming galaxy.

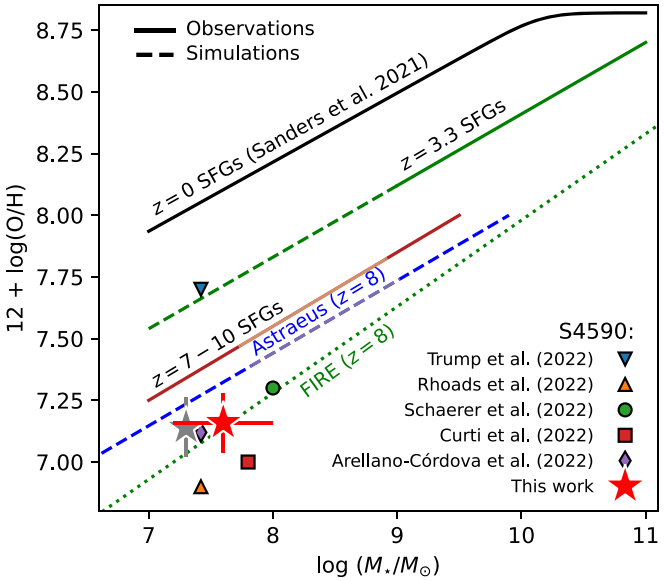

Figure 2. MZ relation of S04590. For comparison, we show the various preexisting MZ estimates for S04590 from the literature, which highlights the uncertainties from the various methods used. We also show various MZ relations either observed for galaxies at $z \approx 0$ and $z \approx 3.3$ (black and green, respectively; Sanders et al. 2021) and at $z \approx 7$–10 (Heintz et al. 2022b) or predicted from the Astraeus (Ucci et al. 2023) and FIRE (Ma et al. 2016) simulations, extrapolated to $z \approx 8$. The local, metal-poor galaxy I Zw 18 is marked by a gray star symbol, showing an MZ relation consistent with that of S04590. Both are consistent with the predictions for high-z MZ relations.

We find that the combined mass and metallicity of S04590 is consistent with those predicted from the Astraeus (Ucci et al. 2023) and Feedback in Realistic Environments (FIRE) (Ma et al. 2016) simulations, extrapolated to $z \approx 8$ (see Figure 2), but slightly lower than the recently observed mass–metallicity (MZ) relation of galaxies at $z \approx 7$–10 (Heintz et al. 2022b). We note that none of the empirical calibrations of the fundamental SFR–Z–$M_\star$ plane relation derived for galaxies at $z \approx 0$–3 (e.g., Curti et al. 2020; Sanders et al. 2021; Li et al. 2022) are able to recover the derived low metallicity of S04590 (see, e.g., Curti et al. 2023). Our SFR and $M_\star$ measurements for instance predict $12 + \log(\mathrm{O/H}) = 7.76$, about 0.6 dex higher than that derived from the strong-line diagnostics. This offset appears to be ubiquitous in high-z galaxies at $z \gtrsim 5$ (Heintz et al. 2022b), likely indicating substantial infall of neutral, pristine gas diluting the metallicity at $z \gtrsim 5$. Intriguingly, S04590 shows a pair of mass and metallicity measurements similar to those of the local, extremely metal-poor galaxy I Zwicky 18 (I Zw 18), which is characterized by an oxygen abundance of $12 + \log(\mathrm{O/H}) = 7.14$ and $M_\star = 2 \times 10^7\ M_\odot$ (Madden et al. 2013).

Determining the gas-phase metallicity from the description by Jones et al. (2020, their Equation (2)) relying on the FIR [O III] 88 μm transition yields $12 + \log(\mathrm{O/H}) = 7.82$. This method thus overpredicts the metallicity by 0.65 dex as compared to the results based on the direct T_e method derived from the redshifted optical nebular and auroral emission lines here. Comparing this metallicity to other strong-line diagnostics defined for local "analogs" of high-redshift galaxies (Bian et al. 2018) yields offsets of −0.2, 0.4, and −0.3 dex for the

R23, O32, and O3Hβ calibrations, respectively. The most accurate calibration for this particular galaxy seems to be the O32 calibration from the Sloan Digital Sky Survey reference sample in Bian et al. (2018), similar to the O32 diagnostics derived by Curti et al. (2020), which seems to be consistent with the direct metallicity within 0.1 dex (as is also evident from the galaxy at $z = 9.5$ presented by Heintz et al. 2022b).

3.4. The Total Dynamical Mass

Assuming that [C II] traces the ISM of S04590 we can further derive the total dynamical mass $M_{\rm dyn}$ of this galaxy. We caution, however, that the spectroscopic blueshift and the $\approx 2\sigma$ spatial offset of [C II] relative to the UV component and [O III] emission (Fujimoto et al. 2022b) indicate that the origin of the [C II] emission is not fully co-spatial with the most intense, star-forming region of the galaxy. Such extended, blueshifted [C II] emission has been observed in other high-z galaxies, and may hint at an offset an abundant gas reservoir, a shock-heated outflowing gas, or minor mergers (e.g., Maiolino et al. 2015; Kohandel et al. 2019; Arata et al. 2020; Akins et al. 2022; Katz et al. 2022). The latter scenario would typically produce much broader (>1000 km s^{-1}) [C II] line profiles (Appleton et al. 2013), whereas the observed narrow-line feature is consistent with the low stellar mass of S04590. We also caution that we are not able to firmly exclude the presence of a merging system due to the limited spatial resolution of our ALMA observations (Rizzo et al. 2022). However, given that the [C II] line width and luminosity are consistent with predictions based on the stellar mass and SFR of S04590, we assume in the following that the [C II] emission is physically associated with the ISM of the galaxy.

We infer $M_{\rm dyn}$ based on the measured FWHM of the [C II] emission line corrected by the instrumental resolution, $\mathrm{FWHM}_{\rm [CII]} = 114 \pm 35$ km s^{-1}, as

$$M_{\rm dyn} = 1.16 \times 10^5 v_{\rm circ}^2 D_{\rm [CII]} \quad (2)$$

following, e.g., Wang et al. (2013) and Willott et al. (2015). Here we approximate the circular velocity to $v_{\rm circ} \approx 0.52 \times \mathrm{FWHM}_{\rm [CII]}$, appropriate for velocities dominated by nonordered rotation (Decarli et al. 2018; Neeleman et al. 2021). Fujimoto et al. (2022b) measured a circularized [C II] effective radius of $0\farcs69 \pm 0\farcs42$ in the image plane, which corresponds to $0\farcs23 \pm 0\farcs14$ in the source plane or to a physical size of $r_{\rm e,[CII]} = 1.1 \pm 0.7$ kpc at $z = 8.496$. Such extended [C II] halos reaching beyond the UV components of the galaxies are typically observed at $z \gtrsim 6$, with $r_{\rm e,[CII]} \approx 2-3 \times r_{\rm e,UV}$ (Smit et al. 2018; Fujimoto et al. 2019; Matthee et al. 2019; Carniani et al. 2020; Akins et al. 2022; Fudamoto et al. 2022), though S04590 presents one of the most notable cases with $r_{\rm e,[CII]} \approx 10 \times r_{\rm e,UV}$. Assuming the "disk" diameter is $D_{\rm [CII]} = 2 \times r_{\rm e,[CII]}$, we infer $D_{\rm [CII]} = 2.2 \pm 1.4$ kpc. This yields a dynamical mass of $M_{\rm dyn} = (9.0 \pm 4.5) \times 10^8\, M_\odot$. We note that if we assume ordered, rotation-dominated motion and an average inclination angle of 45°, the dynamical mass increases by $\approx$50%. However, since there is no strong evidence of ordered motion in S04590, we adopt the above-derivedvalue for the dynamical mass.

4. The Gas, Dust, and Metal Content

4.1. Disentangling the Baryonic Matter Budget

Based on the assumption that the dynamical mass is dominated by the baryonic matter content within the [C II]-emitting region (which is confirmed to be the case for dusty, massive galaxies at $z \sim 4$–5; Rizzo et al. 2020, 2021), the total dynamical mass of S04590 subtracted by its stellar mass should represent the total gas content of this galaxy (in molecular and/or neutral, atomic form); $M_{\rm gas} = M_{\rm dyn} - M_\star$. For S04590, the stellar mass derived from the SED fitting only constitutes $\approx$1%–2% of the total dynamical mass, such that $M_{\rm gas} \approx M_{\rm dyn}$. However, using more conservative estimates of $M_\star \approx 10^8\, M_\odot$ derived from more complex SFHs or spatially resolved analyses (Giménez-Arteaga et al. 2022; Tacchella et al. 2022), we estimate a total gas mass of $M_{\rm gas} = (8.0 \pm 4.0) \times 10^8\, M_\odot$. This yields a gas mass excess and gas fraction of $\log(M_{\rm gas}/M_\star) = 0.9$–$1.7$ and $f_{\rm gas} = M_{\rm gas}/(M_{\rm gas} + M_\star) \gtrsim 90\%$. This gas mass excess is substantial but not too surprising given the overall increase of $M_{\rm gas}/M_\star$ with increasing redshift (Geach et al. 2011; Carilli & Walter 2013; Tacconi et al. 2013; Scoville et al. 2017; Tacconi et al. 2018; Heintz et al. 2021, 2022a) and decreasing metallicity (Catinella et al. 2018; Heintz et al. 2021; Stark et al. 2021).

In Figure 3 we show the total gas mass excess and gas depletion of S04590 together with a set of literature data as a function of redshift. We include the local sample of galaxies at $z \sim 0$ by Leroy et al. (2008), for which we estimate $M_{\rm gas} = M_{\rm HI} + M_{\rm H_2}$. At high z ($z \gtrsim 4$), we compile galaxy samples for which the dynamical mass and the [C II]-emitting size can be inferred, which include the ALMA-ALPINE survey ($z \sim 4$–6; Béthermin et al. 2020; Faisst et al. 2020; Le Fevre et al. 2020), the sample from Capak et al. (2015; $z \sim 5$–6), and ALMA-REBELS ($z \sim 6$–8; Bouwens et al. 2022). These all target "regular" star-forming galaxies at the respective survey redshifts. To estimate $M_{\rm gas}$ for the high-z sample compilation, we again assume $M_{\rm gas} = M_{\rm dyn} - M_\star$ with $M_{\rm dyn}$ estimated using Equation (2) and $M_\star$ as provided in the catalogs. If they are not reported, we assume inclination angles of 45° for the [C II]-emitting galaxy compilation. We observe a strong increase in the gas mass excess as a function of redshift, with averages of $\log(M_{\rm gas}/M_\star) = -0.3$ at $z \approx 0$ and $\log(M_{\rm gas}/M_\star) = 0.7$ at $z \approx 6$–8. Similarly, we compute the gas depletion times for the compiled galaxy samples and find averages of $t_{\rm depl} = 7$ Gyr at $z \approx 0$, declining to $t_{\rm depl} = 0.2$ Gyr at $z \gtrsim 4$. In both cases, S04590 is a clear outlier owing to its large inferred gas mass. However, this can naturally be explained by its low metallicity and stellar mass, for which a large gas fraction is expected, as shown in Figure 4, which are consistent with the properties of I Zw 18.

We now attempt to further disentangle the baryonic mass components of S04590 by estimating the contributions from the cold molecular and neutral atomic gas phases to the total gas mass. Recently, Zanella et al. (2018) calibrated the [C II] luminosity to the total molecular gas mass $M_{\rm mol}$ for a set of galaxies at lower redshifts ($z \sim 0$–2). They found a conversion factor of $\alpha_{\rm [CII]} = \text{[C II]-to-}M_{\rm mol} = 30\, M_\odot/L_\odot$ with a scatter of 0.3 dex (see also Madden et al. 2020), independent of the metallicity. Simulations of galaxies at $z \sim 6$ suggest a slightly lower but consistent average conversion of $\alpha_{\rm [CII]} = 18\, M_\odot/L_\odot$ (Vizgan et al. 2022b). Applying these calibrations to $L_{\rm [CII]}$ yields $M_{\rm mol} = (3.0$–$5.0) \times 10^8\, M_\odot$ (depending on the

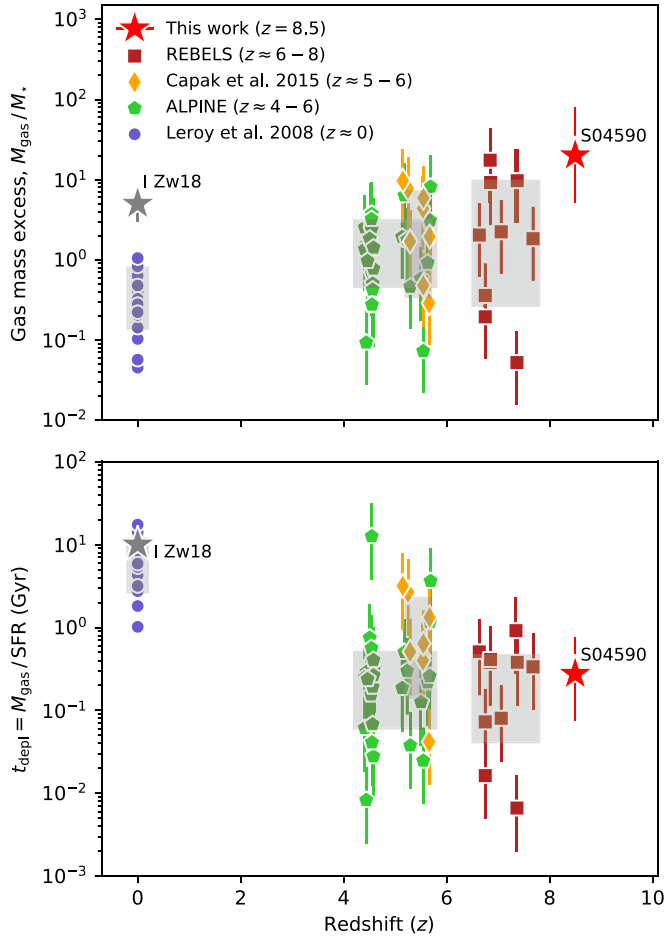

Figure 3. (Top panel) Total gas mass excess, $M_{\rm gas}/M_\star$, as a function of redshift. For the local galaxy sample at $z \sim 0$ (Leroy et al. 2008), $M_{\rm gas} = M_{\rm HI} + M_{\rm H_2}$. For the high-$z$ galaxy sample compilation (see main text for references), we assume that the total gas mass can be estimated as $M_{\rm gas} = M_{\rm dyn,tot} - M_\star$, with $M_{\rm dyn,tot}$ estimated from the [C II] line width and spatial extent. Gray boxes indicate the redshift distributions and standard deviations for each sample. Overall, $M_{\rm gas}/M_\star$ increases with redshift by a factor of $\approx$10 from $z \sim 0$ to $z \sim 7$, and $\log(M_{\rm gas}/M_\star) = 0.9$–$1.7$ for S04590. (Bottom panel) Total gas depletion time, $t_{\rm depl} = M_{\rm gas}/{\rm SFR}$, as a function of redshift; $t_{\rm depl}$ is observed to decrease by a factor of $\approx$10 on average from $z \sim 0$ to $z \sim 7$.

conversion used), with a combined uncertainty of $\approx$40% taking into account the statistical uncertainty and scatter in the calibration. The molecular gas content thus comprises $\approx$30%–50% of $M_{\rm gas}$ by mass.

However, [C II] can also be used as a proxy for the neutral atomic H I gas mass (Heintz et al. 2021, 2022a; Vizgan et al. 2022a) since it has been shown observationally to predominantly originate from the neutral gas phase in the Milky Way and nearby galaxies (Madden et al. 1993, 1997; Pineda et al. 2014; Croxall et al. 2017), with supporting evidence from high-redshift galaxy observations (e.g., Novak et al. 2019; Meyer et al. 2022) and simulations (Katz et al. 2017; Ramos Padilla et al. 2022) as well. We adopt the [C II]-to-H I calibration from Heintz et al. (2021), prescribed as

$$\log \beta_{\rm [CII]} = \log M_{\rm HI}/L_{\rm [CII]} = (-0.87 \pm 0.09) \times \log(Z/Z_\odot) + (1.48 \pm 0.12) \quad (3)$$

(see also Heintz et al. 2022a). In this previous work, the $M_{\rm HI}$ of [C II]-emitting galaxies at $z \sim 6$–8 from REBELS (e.g., Bouwens et al. 2022) could only be inferred based on uncertain metallicity

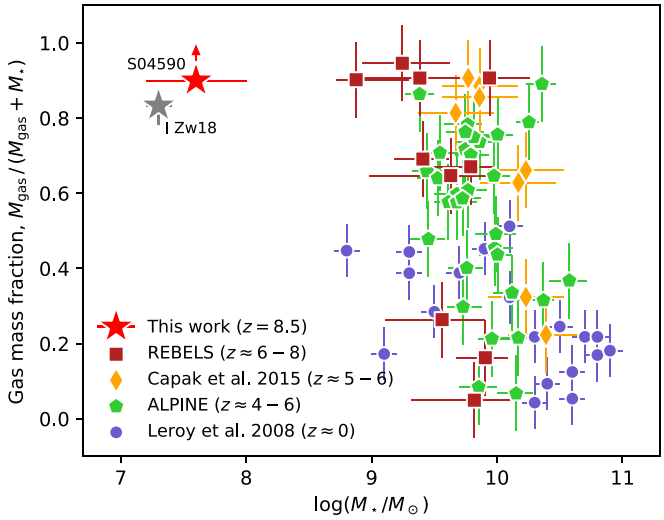

Figure 4. Gas mass fraction, $f_{\rm gas} = M_{\rm gas}/(M_{\rm gas} + M_\star)$, as a function of stellar mass. The symbol notation follows Figure 3. We observe an overall anticorrelation of $f_{\rm gas}$ with stellar mass for both the low- and high-z galaxy samples, though with an offset due to the redshift evolution of $M_{\rm gas}/M_\star$. S04590 and I Zw 18 are both clear outliers, with low stellar masses $M_\star = 1$–$2 \times 10^7\,M_\odot$ and high gas fractions $f_{\rm gas} \gtrsim 90\%$, but seem to follow the overall trend.

estimates assuming an SFR–Z–$M_\star$ fundamental plane relation (e.g., Curti et al. 2020). With the accurate gas-phase metallicity from the NIRSpec analysis performed here, we obtain the first robust high-z $M_{\rm HI}$ estimate of $M_{\rm HI} \approx 10^{10}\,M_\odot$. This is $\approx$10$\times$ more massive than the inferred dynamical mass. This can be explained by (i) the [C II]-to-H I relation being less robust at these high redshifts or low metallicities; (ii) the existence of a much larger H I gas component situated at larger radii than assumed for the [C II]-emitting disk, which then causes the total dynamical mass of the system to be underestimated; or (iii) an increased excitation of $L_{\rm [CII]}$. However, the derived ratio $L_{\rm [CII]}/{\rm SFR} \approx 10^7\,L_\odot/(M_\odot\,{\rm yr}^{-1})$ (see also Fujimoto et al. 2022b) appears consistent with the ubiquitously observed SFR$-L_{\rm [CII]}$ relation (e.g., De Looze et al. 2014; Schaerer et al. 2020). We also note that I Zw 18 again has remarkably comparable properties in terms of the metallicity ($12 + \log({\rm O/H}) = 7.14$), and with an estimated H I gas mass of $M_{\rm HI} = 10^8\,M_\odot$ and [C II] luminosity $L_{\rm [CII]} = 1.1 \times 10^5\,L_\odot$ (e.g., Rémy-Ruyer et al. 2014; Cormier et al. 2015), yielding an equally high [C II]-to-H I ratio of $\log \beta_{\rm [CII]} = \log(M_{\rm HI}/L_{\rm [CII]}) = 2.95\,M_\odot/L_\odot$. In any case, since $M_\star$ and $M_{\rm mol}$ only constitute 2%–10% and 30%–50% of the total dynamical mass of S04590, respectively, we surmise that the largest baryonic mass component is likely in the form of neutral atomic H I gas.

4.2. The Dust and Metal Yield

With the first high-z combination of the gas-phase metallicity and the total gas mass, we can now infer the ISM *metal* mass, $M_{\rm Z,ISM}$, of S04590 at an unprecedented redshift of $z = 8.5$ (previously only possible up to $z \approx 3$; Sanders et al. 2023). We determine this as

$$M_{\rm Z,ISM} = M_{\rm gas} \times 10^{12+\log({\rm O/H})-8.69} \times Z_\odot, \quad (4)$$

where $Z_\odot = 0.0134$ is the solar metallicity by mass. This yields $M_{\rm Z,ISM} = (3.2 \pm 1.5) \times 10^5\,M_\odot$. The expected total Type II

supernova metal production estimated by Peeples et al. (2014), assuming the prescribed SFHs by Leitner (2012) and a nucleosynthetic yield of $y = 0.033$, is $M_{Z,SN} = (7.6 \pm 1.9) \times 10^5\,M_\odot$ marginally consistent with our estimate. Assuming a briefer SFH following Sanders et al. (2023), which is likely more appropriate for S04590 given its high redshift, we obtain consistent results. This indicates that the majority of the produced metals from core-collapse supernovae in S04590 are retained in the ISM. This is in contrast with star-forming galaxies at $z \sim 2$–3, which only retain ≈20% of the produced metals in the ISM (Sanders et al. 2023), and even more so with local galaxies, which have most of their metals captured in stars. Further, this puts strong constraints on the possibility of significant outflows in S04590, as most of the produced metals appear to still be confined to the ISM.

In combination with the constraints placed on the dust mass of $M_d < 1.2 \times 10^5\,M_\odot$ utilizing the FIR continuum coverage provided by ALMA from Fujimoto et al. (2022b), we further determine upper bounds on the mass ratios of the dust-to-gas (DTG, $M_d/M_{\rm gas}$) and dust-to-metal (DTM, M_d/M_Z) content of S04590. We find logDTG < -3.8 and logDTM < -0.5, as also shown in Figure 5. These DTG and DTM mass ratios are substantially lower than the Milky Way average of DTG $\approx 10^{-2}$ and DTM ≈ 0.5. However, this is likely due to the metallicity dependence of the DTG and DTM ratios predicted from simulations (Popping et al. 2017; Hou et al. 2019; Li et al. 2019; Vijayan et al. 2019; Graziani et al. 2020; Triani et al. 2020) and those observed in local galaxies (Rémy-Ruyer et al. 2014; De Vis et al. 2019) and high-z sightlines in absorption (De Cia et al. 2016; Wiseman et al. 2017; Péroux & Howk 2020; Popping & Péroux 2022). Comparing our measurements to those on the DUSTPEDIA[29] sample of local galaxies at $z \approx 0$ (De Vis et al. 2019) and to absorption-derived ratios from quasar absorption line systems (DLAs) at $z \approx 1$–4 (Péroux & Howk 2020; Popping & Péroux 2022) in Figure 5, we find that they are indeed consistent with the expected evolution with metallicity that appears universal across redshifts. Moreover, these results are again in good agreement with the mass ratios derived for I Zw 18, with an estimated dust mass of $M_{\rm dust} \approx 2 \times 10^3\,M_\odot$ (Cannon et al. 2002), yielding a DTG ratio of 2×10^{-5} and a DTM ratio ≈ 5%. These results highlight the strong deviation of the DTG and DTM mass ratios from the Milky Way average at high redshifts and low metallicities.

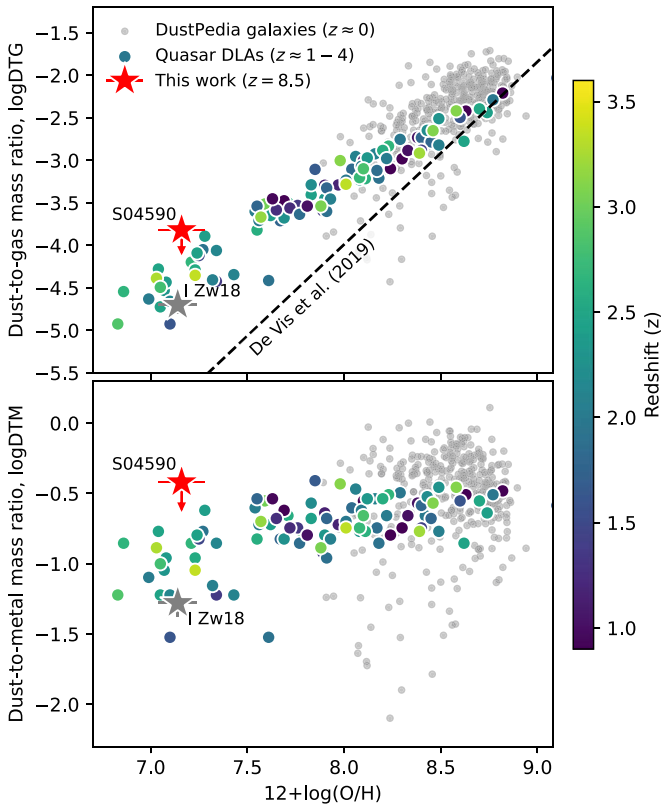

Figure 5. DTG (top) and DTM (bottom) mass ratios as a function of the gas-phase metallicity, 12 + log(O/H). The red and gray star symbols highlight S04590 and I Zw 18, respectively. The gray dots represent the local $z \approx 0$ DUSTPEDIA galaxy sample from De Vis et al. (2019), with their best-fit DTG–metallicity relation shown by the dashed line. The colored filled circles show line-of-sight measurements through quasar absorbers at $z \approx 1$–4 (Péroux & Howk 2020), color-coded as a function of redshift. Both S04590 and I Zw 18 are among the most dust-poor galaxies known, but are consistent with the overall evolution with metallicity.

5. Conclusions

We have presented a comprehensive characterization of the gas, metal, and stellar content of a galaxy at $z_{\rm spec} = 8.496$ (dubbed S04590), providing the most detailed view to date of a galaxy well into the epoch of reionization. These results were enabled by the first joint analysis of the exquisite photometric and spectroscopic observations obtained with the NIRCam, NIRISS, and NIRSpec instruments on board JWST from the early-release science observations (Pontoppidan et al. 2022) and follow-up ALMA observations of the [C II] 158 μm line transition (through the DDT program 2021.A.00022.S, PI: S. Fujimoto). We derived the physical properties of S04590 by modeling the SED of the galaxy and through the strong nebular and auroral emission lines detected in the spectrum. We found that it is a low-mass ($M_\star = 10^{7.2}$–$10^{8.0}\,M_\odot$), low-metallicity (12 +log(O/H) $= 7.16^{+0.10}_{-0.12}$) galaxy, which appears to be overall consistent with predictions for the MZ relation and the SFR$-M_\star$ main sequence at the observed redshift and previous literature estimates, but not with those for the SFR–$M_\star$–Z relation at lower redshifts.

With the simultaneous detection of [C II], we further constrained the dynamics and gas content of the ISM in S04590. First, we determined a total dynamical mass of $M_{\rm dyn} = (9.0 \pm 4.5) \times 10^8\,M_\odot$ based on the [C II] line width. Subtracting the inferred stellar mass, contributing only ≈2%–10% to the total dynamical mass, we determined a total gas mass of $M_{\rm gas} = (8.0 \pm 4.0) \times 10^8\,M_\odot$. S04590 was thus observed to have a gas mass excess and gas fraction of $\log(M_{\rm gas}/M_\star) =$ 0.9–1.7 and $f_{\rm gas} = M_{\rm gas}/(M_{\rm gas} + M_\star) \gtrsim 90\%$, respectively. While these results indicate that S04590 contains one of the most extreme gas fractions derived for high-z galaxies to date, we demonstrated that they are in perfect agreement with the inferred low stellar mass and gas-phase metallicity. We then attempted to disentangle the various gas-phase components through established conversion factors relying on the [C II] line luminosity, for which we inferred $M_{\rm mol} = (3.0$–$5.0) \times 10^8\,M_\odot$ (i.e., 30%–50% of $M_{\rm gas}$). We surmised that the largest contributing factor to the gas mass and the overall baryonic matter budget is thus in the form of

[29] http://dustpedia.astro.noa.gr/

neutral, atomic H I, as supported by recent [C II]-to-H I scaling relations.

With the joint estimates of the gas-phase metallicity and the gas mass, we further estimated the total mass of metals in the ISM of S04590, finding $M_{Z,ISM} = (3.2 \pm 1.6) \times 10^5\,M_\odot$. This is consistent with the expected Type II core-collapse supernova metal yield for the inferred stellar mass buildup. With the independent estimate of the dust mass from the FIR continuum, $M_d < 1.2 \times 10^5\,M_\odot$ (Fujimoto et al. 2022b), we constrained the mass ratios of the DTG and DTM abundance finding logDTG < -3.8 and logDTM < -0.5. This places S04590 as one of the most dust-poor galaxies known to date relative to its inferred gas and metal mass and demonstrates a strong deviation from the typical Milky Way averages in the high-redshift and low-metallicity regimes.

The overall physical properties of S04590 were also found to show remarkable similarity to those of the local, metal-poor galaxy I Zw 18 in terms of the MZ relation, gas fraction, and overall gas, dust, and metal abundance. Generally, this highlights the overall resemblance of the emission line properties of these high-z metal-poor galaxies to local analogs (as also showcased by, e.g., Arellano-Córdova et al. 2022; Katz et al. 2023; Schaerer et al. 2022), and suggests that galaxy properties and their overall evolution are governed by the same fundamental physical processes. With the advent of JWST and in synergy with ALMA, we are now in a position to characterize the stellar, gas, and metal content and constrain how these processes govern the formation and evolution of the first generation of galaxies, as demonstrated by this work.

We would like to thank the referee for providing a constructive response, greatly improving the presentations of the results in this paper. Further, we would like to thank Fengwu Sun for providing insightful comments on an early draft of this project. K.E.H. acknowledges support from the Carlsberg Foundation Reintegration Fellowship Grant CF21-0103 and VILLUM FONDEN through the Villum Experiment Programme. The Cosmic Dawn Center (DAWN) is funded by the Danish National Research Foundation under grant No. 140. T.R.G. acknowledges support from the Carlsberg Foundation (grant No. CF20-0534). K.K acknowledges the support by JSPS KAKENHI Grant Number 17H06130 and the NAOJ ALMA Scientific Research Grant Number 2017-06B.

This work is based in part on observations made with the NASA/ESA/CSA James Webb Space Telescope. The data were obtained from the Mikulski Archive for Space Telescopes (MAST) at the Space Telescope Science Institute, which is operated by the Association of Universities for Research in Astronomy, Inc., under NASA contract NAS 5-03127 for JWST. These observations were obtained as part of the Early Release Observations (ERO) covering the SMACS J0723.3-7327 galaxy cluster. This paper makes use of the following ALMA data: ADS/JAO.ALMA#2021.A.00022.S. ALMA is a partnership of ESO (representing its member states), NSF (USA) and NINS (Japan), together with NRC (Canada), MOST and ASIAA (Taiwan), and KASI (Republic of Korea), in cooperation with the Republic of Chile. The Joint ALMA Observatory is operated by ESO, AUI/NRAO and NAOJ.

Software: This work made use of and acknowledge the following software: `NumPy` (Harris et al. 2020), `Matplotlib` (Hunter 2007), `grizli` (Brammer 2019), `Astrodrizzle` (Hack et al. 2012), CASA (v6.4.1.12; McMullin et al. 2007), NIRSpec analysis tools (v0.3; Brammer 2022), and BAGPIPES (Carnall et al. 2018).

Data Availability Statement

Source codes for the figures and tables presented in this manuscript are available from the corresponding author upon reasonable request. The reduced and calibrated JWST spectroscopic and imaging data are made available on the dedicated repository at https://github.com/keheintz/S04590. The overall JWST data products are available via the Mikulski Archive for Space Telescopes (https://mast.stsci.edu). The specific observations analyzed in this work can be accessed via DOI:10.17909/67ft-nb86.

Appendix A
Best-fit SED Model

As briefly described in the main text, we model the SED of S04590 using BAGPIPES based on the measured JWST/NIRCam+NIRISS photometry. Specifically, we assume a Salim et al. (2018) dust model, allowing the slope (δ) to vary within $-0.9 < \delta < 0.1$, and the 2175 Å bump strength (B) to vary within $0 < B < 3$. We assume Gaussian priors on the various dust parameters. The visual extinction, which we allow to vary in a linear grid between 0 and 2, has the prior centered at 0.1, with a sigma of 0.5, which is the same prior as that for B. For δ, we impose a Gaussian prior centered at -0.5, with a 0.1σ. We also allow the metallicity to vary within $0 < Z < 1$, with a prior centered at 0.2 with a 0.1σ. We assume a Kroupa (2001) IMF. For the constant SFH model, we set the maximum age in a grid from 1 Myr to 10 Myr. Finally, we set the lifetime of birth clouds to 10 Myr. Increasing the maximum age allowed in the prior to 100 Myr we still find the code to infer a mass-weighted age <10 Myr (2.2 ± 0.8 Myr), and the stellar mass remains consistent with the result presented in the main text. We also note that other studies have found consistently young ages, using a similarly constant SFH (Carnall et al. 2023) or a nonparametric SFH (Tacchella et al. 2022). The resulting posterior distributions of the best fit are shown in Figure 6, and summarized in Table 1.

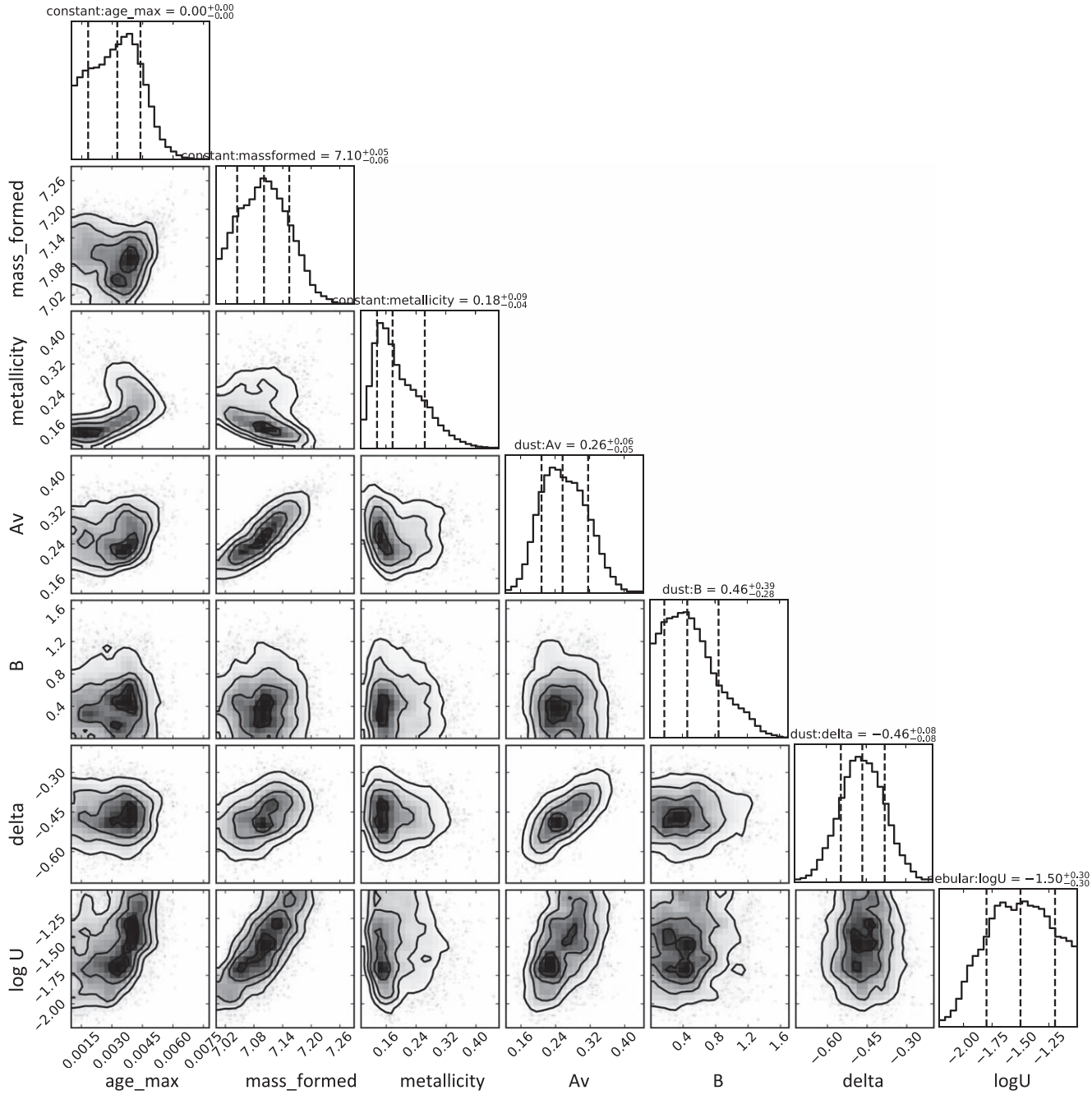

Figure 6. Cornerplot of SED posterior distributions from BAGPIPES.

Appendix B
Line Flux Estimates

In Figure 7 we show regions of our extracted NIRSpec spectrum zoomed in on the relevant nebular and auroral Balmer and oxygen line transitions. Overplotted are the best-fit continuum models and Gaussian profiles used to extract the line fluxes that the main analysis is based on.

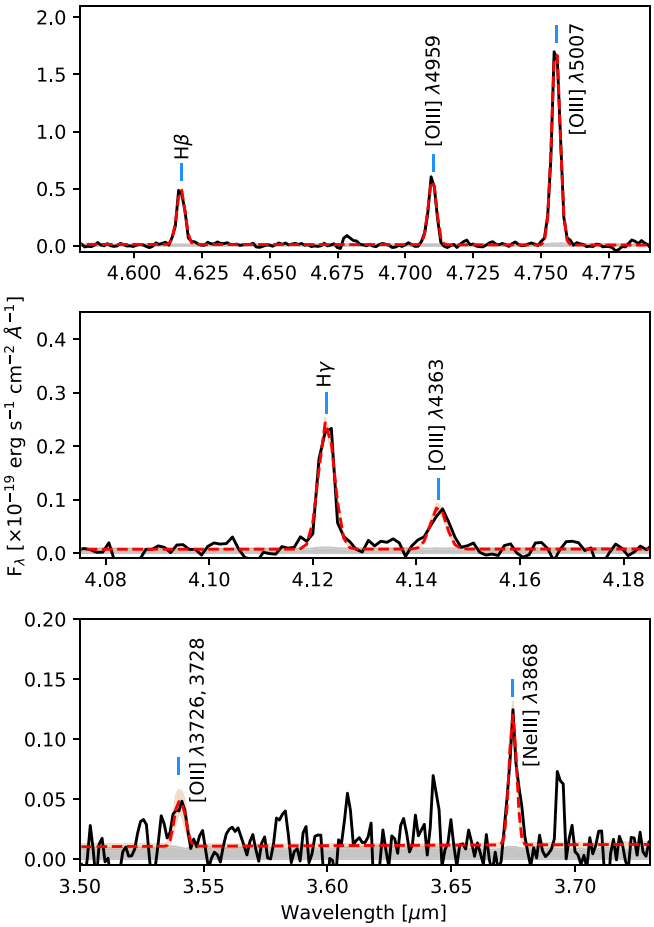

Figure 7. Zoomed-in views of the regions of the spectrum that include the main nebular and auroral emission line transitions examined in this work. The black line shows the flux density, with the gray region represents the noise level. The best-fit continuum and Gaussian profiles to each line transition are shown by the dashed red line. The [O II] $\lambda\lambda$3726, 3728 doublet is not resolved at this spectral resolution.

ORCID iDs

K. E. Heintz https://orcid.org/0000-0002-9389-7413
C. Giménez-Arteaga https://orcid.org/0000-0001-9419-9505
S. Fujimoto https://orcid.org/0000-0001-7201-5066
G. Brammer https://orcid.org/0000-0003-2680-005X
D. Espada https://orcid.org/0000-0002-8726-7685
S. Gillman https://orcid.org/0000-0001-9885-4589
J. González-López https://orcid.org/0000-0003-3926-1411
T. R. Greve https://orcid.org/0000-0002-2554-1837
Y. Harikane https://orcid.org/0000-0002-6047-430X
B. Hatsukade https://orcid.org/0000-0001-6469-8725
K. K. Knudsen https://orcid.org/0000-0002-7821-8873
A. M. Koekemoer https://orcid.org/0000-0002-6610-2048
K. Kohno https://orcid.org/0000-0002-4052-2394
V. Kokorev https://orcid.org/0000-0002-5588-9156
M. M. Lee https://orcid.org/0000-0002-2419-3068
G. E. Magdis https://orcid.org/0000-0002-4872-2294
E. J. Nelson https://orcid.org/0000-0002-7524-374X
F. Rizzo https://orcid.org/0000-0001-9705-2461
R. L. Sanders https://orcid.org/0000-0003-4792-9119
D. Schaerer https://orcid.org/0000-0001-7144-7182
A. E. Shapley https://orcid.org/0000-0003-3509-4855
V. B. Strait https://orcid.org/0000-0002-6338-7295
S. Toft https://orcid.org/0000-0003-3631-7176
F. Valentino https://orcid.org/0000-0001-6477-4011
A. van der Wel https://orcid.org/0000-0002-5027-0135
A. P. Vijayan https://orcid.org/0000-0002-1905-4194
D. Watson https://orcid.org/0000-0002-4465-8264
F. E. Bauer https://orcid.org/0000-0002-8686-8737
S. N. Wilson https://orcid.org/0000-0002-4960-8223

References

Akins, H. B., Fujimoto, S., Finlator, K., et al. 2022, ApJ, 934, 64
Algera, H. S. B., Inami, H., Oesch, P. A., et al. 2023, MNRAS, 518, 6142
Appleton, P. N., Guillard, P., Boulanger, F., et al. 2013, ApJ, 777, 66
Arata, S., Yajima, H., Nagamine, K., Abe, M., & Khochfar, S. 2020, MNRAS, 498, 5541
Arellano-Córdova, K. Z., Berg, D. A., Chisholm, J., et al. 2022, ApJL, 940, L23
Asplund, M., Grevesse, N., Sauval, A. J., & Scott, P. 2009, ARA&A, 47, 481
Bakx, T. J. L. C., Sommovigo, L., Carniani, S., et al. 2021, MNRAS, 508, L58
Bakx, T. J. L. C., Zavala, J. A., Mitsuhashi, I., et al. 2023, MNRAS, 519, 5076
Baldwin, J. A., Phillips, M. M., & Terlevich, R. 1981, PASP, 93, 5
Béthermin, M., Fudamoto, Y., Ginolfi, M., et al. 2020, A&A, 643, A2
Bian, F., Kewley, L. J., & Dopita, M. A. 2018, ApJ, 859, 175
Bouwens, R. J., Smit, R., Schouws, S., et al. 2022, ApJ, 931, 160
Brammer, G. 2019, Grizli: Grism redshift and line analysis software, Astrophysics Source Code Library, record ascl:1905.001
Brammer, G. 2022, msaexp: NIRSpec analyis tools, Zenodo, doi:10.5281/zenodo.7299500
Brinchmann, J. 2022, arXiv:2208.07467
Calzetti, D., Armus, L., Bohlin, R. C., et al. 2000, ApJ, 533, 682
Caminha, G. B., Suyu, S. H., Mercurio, A., et al. 2022, A&A, 666, L9
Cannon, J. M., Skillman, E. D., Garnett, D. R., & Dufour, R. J. 2002, ApJ, 565, 931
Capak, P. L., Carilli, C., Jones, G., et al. 2015, Natur, 522, 455
Carilli, C. L., & Walter, F. 2013, ARA&A, 51, 105
Carnall, A. C., Begley, R., McLeod, D. J., et al. 2023, MNRAS, 518, L45
Carnall, A. C., McLure, R. J., Dunlop, J. S., & Dave, R. 2018, MNRAS, 480, 4379
Carniani, S., Ferrara, A., Maiolino, R., et al. 2020, MNRAS, 499, 5136
Catinella, B., Saintonge, A., Janowiecki, S., et al. 2018, MNRAS, 476, 875
Chabrier, G. 2003, PASP, 115, 763
Christensen, L., Laursen, P., Richard, J., et al. 2012, MNRAS, 427, 1973
Cormier, D., Madden, S. C., Lebouteiller, V., et al. 2015, A&A, 578, A53
Croxall, K. V., Smith, J. D., Pellegrini, E., et al. 2017, ApJ, 845, 96
Curti, M., D'Eugenio, F., Carniani, S., et al. 2023, MNRAS, 518, 425
Curti, M., Mannucci, F., Cresci, G., & Maiolino, R. 2020, MNRAS, 491, 944
Dayal, P., & Ferrara, A. 2018, PhR, 780, 1
Dayal, P., Ferrara, A., Sommovigo, L., et al. 2022, MNRAS, 512, 989
De Cia, A., Ledoux, C., Mattsson, L., et al. 2016, A&A, 596, A97
De Looze, I., Cormier, D., Lebouteiller, V., et al. 2014, A&A, 568, A62
De Vis, P., Jones, A., Viaene, S., et al. 2019, A&A, 623, A5
Decarli, R., Walter, F., Venemans, B. P., et al. 2018, ApJ, 854, 97
Dessauges-Zavadsky, M., Ginolfi, M., Pozzi, F., et al. 2020, A&A, 643, A5
Draine, B. T., & Li, A. 2007, ApJ, 657, 810
Faisst, A. L., Schaerer, D., Lemaux, B. C., et al. 2020, ApJS, 247, 61
Ferland, G. J., Chatzikos, M., Guzmán, F., et al. 2017, RMxAA, 53, 385
Ferrara, A., Sommovigo, L., Dayal, P., et al. 2022, MNRAS, 512, 58
Fudamoto, Y., Smit, R., Bowler, R. A. A., et al. 2022, ApJ, 934, 144
Fujimoto, S., Finkelstein, S. L., Burgarella, D., et al. 2022a, arXiv:2211.03896
Fujimoto, S., Ouchi, M., Ferrara, A., et al. 2019, ApJ, 887, 107
Fujimoto, S., Ouchi, M., Nakajima, K., et al. 2022b, arXiv:2212.06863
Geach, J. E., Smail, I., Moran, S. M., et al. 2011, ApJL, 730, L19
Gillman, S., Puglisi, A., Dudzevičiūtė, U., et al. 2022, MNRAS, 512, 3480
Giménez-Arteaga, C., Oesch, P. A., Brammer, G. B., et al. 2022, arXiv:2212.08670
Graziani, L., Schneider, R., Ginolfi, M., et al. 2020, MNRAS, 494, 1071
Hack, W. J., Dencheva, N., Fruchter, A. S., et al. 2012, AAS Meeting, 220, 135.15
Harikane, Y., Ouchi, M., Oguri, M., et al. 2022, arXiv:2208.01612
Harris, C. R., Millman, K. J., van der Walt, S. J., et al. 2020, Natur, 585, 357
Hartoog, O. E., Malesani, D., Fynbo, J. P. U., et al. 2015, A&A, 580, A139
Hashimoto, T., Laporte, N., Mawatari, K., et al. 2018, Natur, 557, 392
Heintz, K. E., Brammer, G. B., Giménez-Arteaga, C., et al. 2022b, arXiv:2212.02890
Heintz, K. E., Oesch, P. A., Aravena, M., et al. 2022a, ApJL, 934, L27
Heintz, K. E., Watson, D., Oesch, P. A., Narayanan, D., & Madden, S. C. 2021, ApJ, 922, 147
Hollenbach, D. J., & Tielens, A. G. G. M. 1999, RvMP, 71, 173
Horne, K. 1986, PASP, 98, 609
Hou, K.-C., Aoyama, S., Hirashita, H., Nagamine, K., & Shimizu, I. 2019, MNRAS, 485, 1727
Hunt, L. K., & Hirashita, H. 2009, A&A, 507, 1327
Hunter, J. D. 2007, CSE, 9, 90
Inami, H., Algera, H. S. B., Schouws, S., et al. 2022, MNRAS, 515, 3126
Izotov, Y. I., Stasińska, G., Meynet, G., Guseva, N. G., & Thuan, T. X. 2006, A&A, 448, 955
Jakobsen, P., Ferruit, P., Alves de Oliveira, C., et al. 2022, A&A, 661, A80
Jones, T., Sanders, R., Roberts-Borsani, G., et al. 2020, ApJ, 903, 150
Katz, H., Kimm, T., Sijacki, D., & Haehnelt, M. G. 2017, MNRAS, 468, 4831
Katz, H., Rosdahl, J., Kimm, T., et al. 2022, MNRAS, 510, 5603
Katz, H., Saxena, A., Cameron, A. J., et al. 2023, MNRAS, 518, 592
Kewley, L. J., & Ellison, S. L. 2008, ApJ, 681, 1183
Kewley, L. J., Nicholls, D. C., & Sutherland, R. S. 2019, ARA&A, 57, 511
Knudsen, K. K., Richard, J., Kneib, J.-P., et al. 2016, MNRAS, 462, L6
Kohandel, M., Pallottini, A., Ferrara, A., et al. 2019, MNRAS, 487, 3007
Kroupa, P. 2001, MNRAS, 322, 231
Lagache, G., Cousin, M., & Chatzikos, M. 2018, A&A, 609, A130
Le Fevre, O., Bethermin, M., Faisst, A., et al. 2020, A&A, 643, A1
Leitner, S. N. 2012, ApJ, 745, 149
Leroy, A. K., Walter, F., Brinks, E., et al. 2008, AJ, 136, 2782
Li, M., Cai, Z., Bian, F., et al. 2022, arXiv:2211.01382
Li, Q., Narayanan, D., & Dave, R. 2019, MNRAS, 490, 1425
Ma, X., Hopkins, P. F., Faucher-Giguère, C.-A., et al. 2016, MNRAS, 456, 2140
Madden, S. C., Cormier, D., Hony, S., et al. 2020, A&A, 643, A141
Madden, S. C., Geis, N., Genzel, R., et al. 1993, ApJ, 407, 579
Madden, S. C., Poglitsch, A., Geis, N., Stacey, G. J., & Townes, C. H. 1997, ApJ, 483, 200
Madden, S. C., Remy-Ruyer, A., Galametz, M., et al. 2013, PASP, 125, 600
Mahler, G., Jauzac, M., Richard, J., et al. 2022, arXiv:2207.07101
Maiolino, R., & Mannucci, F. 2019, A&ARv, 27, 3
Maiolino, R., Carniani, S., Fontana, A., et al. 2015, MNRAS, 452, 54
Matthee, J., Sobral, D., Boogaard, L. A., et al. 2019, ApJ, 881, 124
McMullin, J. P., Waters, B., Schiebel, D., Young, W., & Golap, K. 2007, in ASP Conf. Ser. 376, Astronomical Data Analysis Software and Systems XVI, ed. R. A. Shaw, F. Hill, & D. J. Bell (San Francisco, CA: ASP), 127
Meyer, R. A., Walter, F., Cicone, C., et al. 2022, ApJ, 927, 152
Nakajima, K., Ouchi, M., Isobe, Y., et al. 2023, arXiv:2301.12825
Neeleman, M., Novak, M., Venemans, B. P., et al. 2021, ApJ, 911, 141
Novak, M., Bañados, E., Decarli, R., et al. 2019, ApJ, 881, 63

Osterbrock, D. E., & Ferland, G. J. 2006, Astrophysics of Gaseous Nebulae and Active Galactic Nuclei (Sausalito, CA: Univ. Science Books)
Pacifici, C., Iyer, K. G., Mobasher, B., et al. 2022, arXiv:2212.01915
Peeples, M. S., Werk, J. K., Tumlinson, J., et al. 2014, ApJ, 786, 54
Peng, C. Y., Ho, L. C., Impey, C. D., & Rix, H.-W. 2002, AJ, 124, 266
Péroux, C., & Howk, J. C. 2020, ARA&A, 58, 363
Pineda, J. L., Langer, W. D., & Goldsmith, P. F. 2014, A&A, 570, A121
Planck Collaboration, Aghanim, N., Akrami, Y., et al. 2020, A&A, 641, A6
Pontoppidan, K., Blome, C., Braun, H., et al. 2022, ApJL, 936, L14
Popping, G. 2023, A&A, 669, L8
Popping, G., & Péroux, C. 2022, MNRAS, 513, 1531
Popping, G., Somerville, R. S., & Galametz, M. 2017, MNRAS, 471, 3152
Ramos Padilla, A. F., Wang, L., van der Tak, F. F. S., & Trager, S. 2022, arXiv:2205.11955
Reddy, N. A., Oesch, P. A., Bouwens, R. J., et al. 2018, ApJ, 853, 56
Rémy-Ruyer, A., Madden, S. C., Galliano, F., et al. 2014, A&A, 563, A31
Rhoads, J. E., Wold, I. G. B., Harish, S., et al. 2023, ApJL, 942, L14
Rizzo, F., Kohandel, M., Pallottini, A., et al. 2022, A&A, 667, A5
Rizzo, F., Vegetti, S., Fraternali, F., Stacey, H. R., & Powell, D. 2021, MNRAS, 507, 3952
Rizzo, F., Vegetti, S., Powell, D., et al. 2020, Natur, 584, 201
Robertson, B. E. 2022, ARA&A, 60, 121
Saccardi, A., Vergani, S. D., De Cia, A., et al. 2022, arXiv:2211.16524
Salim, S., Boquien, M., & Lee, J. C. 2018, ApJ, 859, 11
Sanders, R. L., Shapley, A. E., Jones, T., et al. 2021, ApJ, 914, 19
Sanders, R. L., Shapley, A. E., Jones, T., et al. 2023, ApJ, 942, 24
Schaerer, D., Ginolfi, M., Béthermin, M., et al. 2020, A&A, 643, A3
Schaerer, D., Marques-Chaves, R., Oesch, P., et al. 2022, A&A, 665, L4
Scoville, N., Aussel, H., Sheth, K., et al. 2014, ApJ, 783, 84
Scoville, N., Lee, N., Bout, P. V., et al. 2017, ApJ, 837, 150
Simcoe, R. A., Onoue, M., Eilers, A.-C., et al. 2020, arXiv:2011.10582
Smit, R., Bouwens, R. J., Carniani, S., et al. 2018, Natur, 553, 178
Solomon, P. M., & Vanden Bout, P. A. 2005, ARA&A, 43, 677
Sommovigo, L., Ferrara, A., Carniani, S., et al. 2021, MNRAS, 503, 4878
Sommovigo, L., Ferrara, A., Pallottini, A., et al. 2022, MNRAS, 513, 3122
Speagle, J. S., Steinhardt, C. L., Capak, P. L., & Silverman, J. D. 2014, ApJS, 214, 15
Stacey, G. J., Geis, N., Genzel, R., et al. 1991, ApJ, 373, 423
Stark, D. V., Masters, K. L., Avila-Reese, V., et al. 2021, MNRAS, 503, 1345
Stefanon, M., Bouwens, R. J., Labbé, I., et al. 2022, ApJ, 927, 48
Sugahara, Y., Inoue, A. K., Fudamoto, Y., et al. 2022, ApJ, 935, 119
Tacchella, S., Johnson, B. D., Robertson, B. E., et al. 2022, arXiv:2208.03281
Tacconi, L. J., Genzel, R., Saintonge, A., et al. 2018, ApJ, 853, 179
Tacconi, L. J., Neri, R., Genzel, R., et al. 2013, ApJ, 768, 74
Taylor, A. J., Barger, A. J., & Cowie, L. L. 2022, ApJL, 939, L3
Topping, M. W., Stark, D. P., Endsley, R., et al. 2022, MNRAS, 516, 975
Triani, D. P., Sinha, M., Croton, D. J., Pacifici, C., & Dwek, E. 2020, MNRAS, 493, 2490
Trump, J. R., Arrabal Haro, P., Simons, R. C., et al. 2022, arXiv:2207.12388
Ucci, G., Dayal, P., Hutter, A., et al. 2023, MNRAS, 518, 3557
Vijayan, A. P., Clay, S. J., Thomas, P. A., et al. 2019, MNRAS, 489, 4072
Vizgan, D., Greve, T. R., Olsen, K. P., et al. 2022b, ApJ, 929, 92
Vizgan, D., Heintz, K. E., Greve, T. R., et al. 2022a, ApJL, 939, L1
Wang, R., Wagg, J., Carilli, C. L., et al. 2013, ApJ, 773, 44
Whitler, L., Stark, D. P., Endsley, R., et al. 2023, MNRAS, 519, 5859
Willott, C. J., Bergeron, J., & Omont, A. 2015, ApJ, 801, 123
Wiseman, P., Schady, P., Bolmer, J., et al. 2017, A&A, 599, A24
Wolfire, M. G., McKee, C. F., Hollenbach, D., & Tielens, A. G. G. M. 2003, ApJ, 587, 278
Yoon, I., Carilli, C. L., Fujimoto, S., et al. 2022, arXiv:2210.08413
Zanella, A., Daddi, E., Magdis, G., et al. 2018, MNRAS, 481, 1976